Journal of Materials Chemistry A

Accepted Manuscript

This article can be cited before page numbers have been issued, to do this please use: X. Chen, Y. Qiu, G. Liu, W. zheng, W. Feng, F. Gao, W. Cao, Y. Q. Fu, W. Hu and P. Hu, *J. Mater. Chem. A*, 2017, DOI: 10.1039/C7TA02327H.

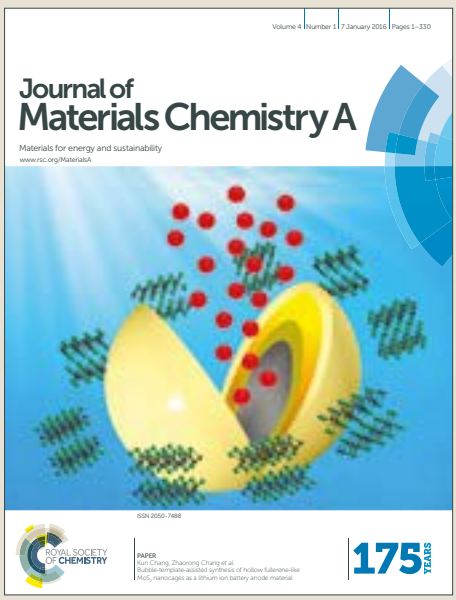

ROYAL SOCIETY OF CHEMISTRY

rsc.li/materials-a

DOI: 10.1039/C7TA02327H

Journal Name

ARTICLE

Tuning electrochemical catalytic activity of defective 2D terrace $MoSe_2$ heterogeneous catalyst *via* cobalt doping†

Received 00th January 20xx,
Accepted 00th January 20xx

DOI: 10.1039/x0xx00000x

www.rsc.org/

Xiaoshuang Chen,[ab] Yunfeng Qiu,[a] Guangbo Liu,[a] Wei Zheng,[a] Wei Feng,[a] Feng Gao,[a] Wenwu Cao,[c] Yongqing Fu,*[d] Wenping Hu*[be] and PingAn Hu*[a]

This study presents successful growth of defective 2D terrace $MoSe_2$/CoMoSe lateral heterostructures (LH), bilayer and multilayer $MoSe_2$/CoMoSe LH, and vertical heterostructures (VH) nanolayers by doping metal Co (cobalt) element into $MoSe_2$ atomic layers to form a CoMoSe alloy at the high temperature (~900 °C). After the successful introduction of metal Co heterogeneity in the $MoSe_2$ thin layers, more active sites can be created to enhance hydrogen evolution reaction (HER) activities combining with metal Co catalysis, through the mechanisms including (1) atomic arrangement distortion in CoMoSe alloy nanolayers, (2) atomic level coarsening in LH interfaces and terrace edge layer architecture in VH, (3) formation of defective 2D terrace $MoSe_2$ nanolayers heterogeneous catalyst *via* metal Co doping. The HER investigations indicated that the obtained products with LH and VH exhibited an improved HER activity in comparison with those from the pristine 2D $MoSe_2$ electrocatalyst and LH type $MoSe_2$/CoMoSe. The present work shows a facile yet reliable route to introduce metal ions into ultrathin 2D transition metal dichalcogenides (TMDCS) and produce defective 2D alloy atomic layers for exposing active sites, and thus eventually improve their electrocatalytic performance.

Introduction

Semiconductor heterostructures are the critical platform for many applications such as field effect transistors (FET), photodetectors, solar cells, light-emitting diodes, HER and lasers.[1-6] Traditional heterostructures are principally based on groups IV, II-VI, or III-V semiconductors materials by covalent bonds among atoms in the heterointerfaces.[7] The atomic interfacial diffusion during the reaction process will lead to atomic level coarsening or distortion on the boundary of heterostructures and ingredient modification at the heterostructure interfaces to generate defects, which will be favorable to create more active sites spontaneously for improving the performance of semiconductor heterostructures materials, particularly as the thickness of the materials is reduced to atomic layers.[7,8] Similar to the conventional heterostructures, 2D layered TMDCS heterostructures can be projected and constructed to produce the LH through covalent bonding between atoms on the boundary.[9,10] Moreover, VH can also be fabricated by assembling different and independent 2D TMDCS nanolayer materials into functional and terrace multilayer architectures with van der Waals (vdW) forces, with the dangling bonds on the edges of 2D TMDCS materials.[11,12] The terrace multilayer 2D TMDCS heterostructures will provide more active sites to develop the HER performance, as a result that the edge of pure 2D TMDCS are the main catalytic sites.[13,14]

Under normal circumstances, importing heterogeneous spin states in 2D atomic layers, or doping exotic metal atoms in 2D TMDCS nanolayers crystal lattice, could develop a regional unbalanced Coulomb force. Therefore, the accidental but micromechanically formative chaos will guide slight distortion and defects in the atomic layers due to the atomic re-arrangement, further creating more active sites in 2D materials. These will guarantee the primitive electron conjugated structures on the 2D plane and are beneficial to fast electron transfer for optimizing the HER performance.[15-17] Clearly, the introduction of metal heterogeneous element in 2D TMDCS atomic layers is deemed to an effective method to promote the HER activity of 2D TMDCS materials. Among these 2D TMDCS materials, $MoSe_2$, as a representative 2D material, possesses outstanding electronic and optoelectronic properties.[18-20] In addition, our group has successfully grown $MoSe_2$ atomic layers by a conventional chemical vapor deposition technique on SiO_2/Si substrate, offering an additional platform to realize the above-proposed new idea.[21] Moreover, the functional nanomaterials[22-30] such as Co catalyst have been broadly applied as a category of electrocatalysts, as a result of intrinsic high conductivity of the metal Co element.

[a] Key Lab of Microsystem and Microstructure of Ministry of Education, Harbin Institute of Technology, Harbin 150080, China. E-mail: hupa@hit.edu.cn
[b] Department of Physics, Harbin Institute of Technology, Harbin 150080, China
[c] Condensed Matter Science and Technology Institute, Harbin Institute of Technology, Harbin 150080, China
[d] Faculty of Engineering & Environment, Northumbria University, Newcastle upon Tyne, NE1 8ST, UK
[e] Key Laboratory of Organic Solids, Institute of Chemistry, Chinese Academy of Sciences, Beijing 100190, China. E-mail:huwp@iccas.ac.cn

† Electronic Supplementary Information (ESI) available. See DOI:10.1039/x0xx00000x

View Article Online
DOI: 10.1039/C7TA02327H

Based on the above discussions, we proposed a method, for the first time, to form defective 2D terrace $MoSe_2$/CoMoSe LH, bilayer and multilayer $MoSe_2$/CoMoSe LH and VH nanolayers by heterogeneously doping Co element in $MoSe_2$ nanolayers at high temperature. The mechanisms of Co doping can be explained by (1) distortion and defect generation in the $MoSe_2$ nanolayers; (2) atomic level coarsening and diffusion in LH boundarys; (3) formation of terrace edge layers in VH with the help of metal Co catalysis. Therefore, we have found a new strategy to create more active sites and enhance conductivity of materials for improve the HER activity through the successful introduction of metal Co element in $MoSe_2$ atomic layers, and $MoSe_2$/CoMoSe LH and VH shows outstanding HER performance. The obtained $MoSe_2$/CoMoSe LH and VH yields a low overpotential of ~305 mV at 10 mA cm^{-2}, a smaller Tafel slope of ~95.2 mV/dec, and a good stability, which are comparable to those of the reported HER electrocatalysts made of non-noble-metal 2D TMDCS atomic layers.[6,13,31-33] Even more significant, we believe that this work generate a new manufacture route to dope other metal ions into 2D TMDCS atomic layers in order to fabricate defective 2D terrace alloy nanolayers for further developing LH or VH on different substrates for wide applications.

Experimental

Growth of defective 2D terrace $MoSe_2$/CoMoSe LH and VH on SiO_2/Si substrate

The mixture of MoO_3 powder (150 mg, 99.9 %, Aladdin) and Co_3O_4 powder (300 mg, 99.9 %, Aladdin) was located on the high temperature zone in a quartz furnace for chemical vapor deposition (CVD). And then this high temperature zone was heated to ~750 °C. Simultaneously, selenium (Se) powder (0.6 g, 99.99 %, Aladdin) was put at the low temperature zone of the furnace and heated to ~300 °C and kept for 30 min to obtain triangular $MoSe_2$ monolayers on 300 nm SiO_2/Si substrate. During the growth process, the substrate was placed down-facing onto the mixture of MoO_3 powder and Co_3O_4 powder. Then the high temperature zone is increased to ~900 °C and maintained for different reaction durations to grow CoMoSe alloy along the edge or on the surfaces of $MoSe_2$ triangles. During the entire reaction process, gas mixture of Ar/H_2 (45/15 sccm) was used as the gas carrier and a reducing gas, respectively. In the end, different types of defective 2D terrace $MoSe_2$/CoMoSe LH, LH and VH nanolayers were successful obtained and the furnace was cooled down to room temperature naturally. Schematic illustration of the growth process of the nanolayers is shown in Fig. S1.

Characterization

Defective 2D terrace $MoSe_2$/CoMoSe LH, LH and VH nanolayers and triangular $MoSe_2$ monolayers were characterized by optical microscopy (Leica DM4500P), scanning electron microscope (SEM, Hitachi SU-800, accelerating voltage of 10 kV), Raman spectroscopy (with a wavelength of 532 nm) and photoluminescence (PL) spectroscopy (LabRAM XploRA, incident power of 1 mW, excitement wavelength 532 nm), atomic force microscopy (AFM, Nanoscope IIIa Vecco), X-ray diffraction (XRD, Diffractometer-6000 with Cu Ka radiation with a wavelength λ of 0.1542 nm), X–ray photoelectron spectroscopy (XPS, Thermo Scientific K-Alpha with Al Ka radiation as a probe), transmission electron microscopy (TEM, Tacnai–G2 F30, with an accelerating voltage of 300 kV).

Electrochemical Measurements

All HER measurements were performed in a three-electrode system on an electrochemical station (CHI 660D, Chenhua, China) at room temperature, where a 50 mL of 0.5 M sulfuric acid (H_2SO_4) was used as the electrolyte solution. A piece of platinum, a Ag/AgCl electrode, and the products on glassy carbon (GC) electrode using the solution of Polymethyl Methacrylate (PMMA) to transfer from SiO_2/Si substrate were used as the counter electrode, the reference electrode and working electrodes, respectively. Electrolyte solution was deaerated by nitrogen gas (99.999 % N_2) for 30 min throughout the electrochemical tests except for the Ag/AgCl electrode calibration measurement. Linear sweep voltammetry (LSV) measurements were conducted between 0.2 V and –0.8 V vs reversible hydrogen electrode (RHE) with a scan rate of 5 mV s^{-1}. Cyclic voltammetry (CV) was performed between 0 and –0.5 V vs RHE at 50 mV s^{-1} to evaluate the HER stability. All the potentials were calibrated with respect to the RHE.

Transfer of defective 2D terrace $MoSe_2$/CoMoSe LH and VH nanolayers from SiO_2/Si substrate to Cu TEM grid or GC electrode

The PMMA solution was evenly spin-coated on a 300 nm SiO_2/Si substrate grown with the samples at a spinning speed of 2500 rpm for 35 s. When heated at 80 °C for 15 min, the SiO_2/Si substrate with PMMA thin film was immersed in 4 % HF liquid. And then the samples with the PMMA thin film were separated from the substrate due to the etching function via the HF liquid. Subsequently, the independent PMMA thin film with the products was washed with deionized water and cover on the Cu TEM grid or GC electrode. In the end, the PMMA thin film was removed by acetone, leaving only the samples on Cu TEM grid or GC electrode.

Results and discussion

Fig. 1 displays the schematic illustrations of defective 2D terrace $MoSe_2$/CoMoSe LH, LH and VH nanolayers. In the first

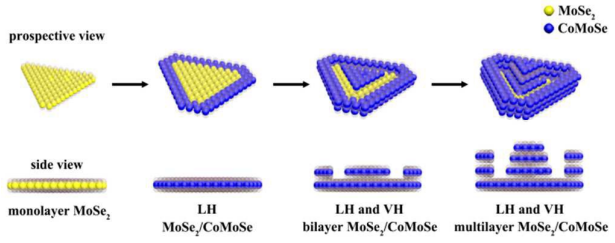

Fig. 1 Schematic illustrations of the formation of defective 2D terrace $MoSe_2$/CoMoSe LH, LH and VH nanolayers.

View Article Online
DOI: 10.1039/C7TA02327H

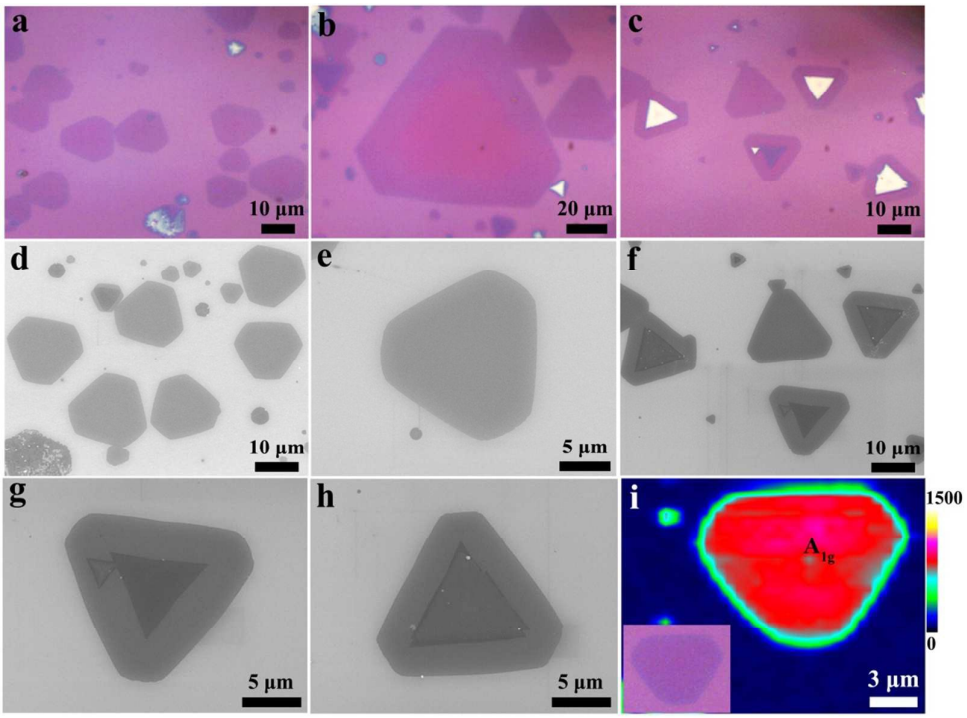

Fig. 2 Optical, SEM and Raman mapping of defective 2D terrace $MoSe_2$/CoMoSe LH, LH and VH nanolayers. (a,b) Optical images of 2D $MoSe_2$/CoMoSe LH nanolayers. (c) Optical image of 2D $MoSe_2$/CoMoSe LH and VH nanolayers. (d,e) SEM images of 2D $MoSe_2$/CoMoSe LH nanolayers. (f-h) SEM images of 2D $MoSe_2$/CoMoSe LH and VH nanolayers. (i) Raman mapping of 2D $MoSe_2$/CoMoSe LH nanolayers.

stage, triangular $MoSe_2$ monolayers were grown on 300 nm SiO_2/Si substrate by chemical vapor deposition method. After $MoSe_2$ growth, the high temperature zone of the furnace was heated to 900 °C. Co_3O_4 powder and MoO_3 powder were simultaneously evaporated to react with the Se powder to form CoMoSe alloy nanolayers. CoMoSe alloy nanolayers were grown along $MoSe_2$ triangle margin to form defective 2D lateral heterostructures of $MoSe_2$/CoMoSe nanolayers due to the edge of $MoSe_2$ triangle possesses rich dangling bonds to encourage the growth of nanolayers. With the increase of reaction time, CoMoSe alloy nanolayers will be grown on the surface of $MoSe_2$ triangles to generate 2D terrace bilayers or multilayer vertical heterostructures of $MoSe_2$/CoMoSe nanolayers. The experimental details are displayed in the Experimental Section.

Optical images in Fig. 2a and b display hexagonal $MoSe_2$/CoMoSe LH nanolayers with the dimensions ranging from ~15 μm to 100 μm. Optical image (Fig. 2b) clearly reveals the $MoSe_2$/CoMoSe LH through optical contrast diversity, with triangular $MoSe_2$ monolayers displaying a pink color and CoMoSe alloy nanolayers as a purple color. The CoMoSe alloy nanolayers were grown along $MoSe_2$ triangle margins at ~ 900 °C for 10 min to produce hexagonal $MoSe_2$/CoMoSe LH nanolayers. However, smaller optical image hardly shows the existence of the $MoSe_2$/CoMoSe LH, due to less CoMoSe alloys along the edges of the triangular $MoSe_2$. Fig. 2c exhibits bilayer (blue color in the middle) and multilayer (light white color in the middle) $MoSe_2$/CoMoSe LH and VH optical images with the dimension of ~15 μm. Low magnification SEM images (Fig. 2d,f) of $MoSe_2$/CoMoSe LH, bilayer or multilayer LH and VH nanolayers with the measurement of ~15 μm are consistent with the results of optical images. Individual high magnification SEM images of $MoSe_2$/CoMoSe LH, bilayer or multilayer LH and VH nanolayers are shown in Fig. 2e, g and f with the different grayscale contrast, respectively. Fig. 2i shows the Raman mapping image of 2D $MoSe_2$/CoMoSe LH with the A_{1g} characteristic peak of $MoSe_2$. The edge of CoMoSe alloy demonstrates a weaker intensity of A_{1g} Raman peak than that in the center of $MoSe_2$, as a result of Co doping in the margin of $MoSe_2$/CoMoSe LH nanolayers.

Fig. 3a displays Raman spectra of 2D LH center ($MoSe_2$ region), LH edge (CoMoSe region), bilayer and multilayer ($MoSe_2$/CoMoSe) VH, which reveal two typical Raman characteristic peaks of $MoSe_2$ at low wavenumber (A_{1g} mode, out-plane vibration) and high wavenumber (E_{2g} mode, in-plane vibration). $MoSe_2$ monolayer region exhibits the A_{1g} mode at 240.3 cm^{-1} and the E_{2g} mode at 288.2 cm^{-1}, respectively. However, as the Co doping and the thickness increase, the A_{1g} mode displays a blue shift to high wavenumber side, suggesting the possible effects of the Co doping and/or the thickness variation on a 2D thin layer structure. According to the reports of the literatures, the Raman spectra of the hexagonal single-crystal MoS_2 possess two major peaks E^1_{2g} and A_{1g} modes (which correspond to the vibrational motions of Mo and S atoms in the *x*-*y* layered plane and two S atoms along the *z*-axis of the unit cell, respectively). The exact peak

View Article Online
DOI: 10.1039/C7TA02327H

positions depend on the layer thickness of the samples. As the thickness decreased, the frequencys of the E^1_{2g} and A_{1g} modes increased and decreased, respectively. These trends can be ascribed to Coulombic interactions and possible stacking-induced changes in intralayer bonding.[34,35] 2D TMDCs $MoSe_2$ and MoS_2 materials have very similar structure and are both assigned to the same kind material. Therefore, the blue shift of the A_{1g} mode in our samples may also be assigned to the thickness variation of the layer structure. With the increase of Co doping and the layer number, the PL peak exhibits a red shift phenomenon. Generally, Raman and PL spectra indicate the high quality of the as-obtained atomic layers of 2D $MoSe_2$/CoMoSe heterostructures.

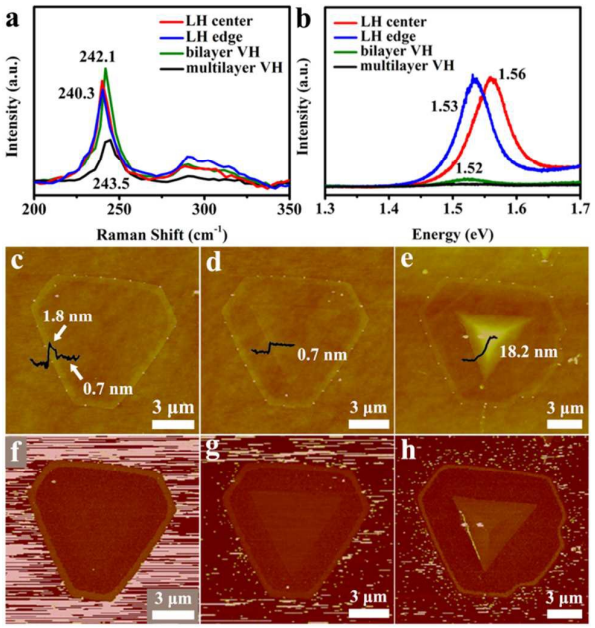

Fig. 3 Raman, PL and AFM characterization of defective 2D terrace $MoSe_2$/CoMoSe LH, LH and VH nanolayers. (a) Raman and (b) PL spectra in 2D $MoSe_2$/CoMoSe LH center, edge, bilayer and multilayer $MoSe_2$/CoMoSe VH. (c-e) AFM height and (f-h) the corresponding AFM phase images of 2D $MoSe_2$/CoMoSe LH, bilayer and multilayer $MoSe_2$/CoMoSe LH and VH nanolayers.

The thicknesses of 2D $MoSe_2$/CoMoSe heterostructures are shown in Fig. 3c-e obtained using AFM technique. The results exhibit that the interior $MoSe_2$ is monolayer of ~0.7 nm and the outside CoMoSe alloy possesses the higher thickness of ~1.8 nm (Fig. 3c) in the $MoSe_2$/CoMoSe LH, because the Co doping can act as a metal catalyst and thus facilitate the growth rate of $MoSe_2$ during the reaction process. Bilayer and multilayer $MoSe_2$/CoMoSe LH and VH nanolayers with the heights of ~1.4 nm (bilayer $MoSe_2$/CoMoSe VH) and 18.9 nm (multilayer $MoSe_2$/CoMoSe VH) are also shown in Fig. 3d and e, respectively. AFM measurement results also show 2D terrace structural patterns with more edge layers. Fig. 3f-h display the corresponding AFM phase images of different type $MoSe_2$/CoMoSe heterostructures, demonstrating that distinct phases by the difference of color contrast are in different regions with various ($MoSe_2$ or CoMoSe) ingredients. These results further prove the successful doping of Co element in $MoSe_2$ atomic layers.

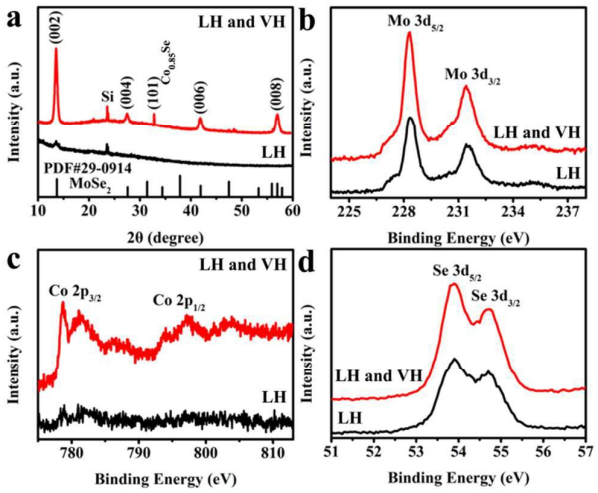

Fig. 4 XRD and XPS characterization of defective 2D terrace $MoSe_2$/CoMoSe LH, LH and VH nanolayers. (a) XRD patterns, (b) Mo 3d, (c) Co 2p and (d) Se 3d XPS spectra.

XRD pattern of 2D $MoSe_2$/CoMoSe LH atomic layers (Fig. 4a, in dark) only displays a hexagonal structure of $MoSe_2$ regardless the Co composition, simply because the content of Co element is very low in the $MoSe_2$/CoMoSe LH. However, XRD pattern of the $MoSe_2$/CoMoSe LH and VH atomic layers (Fig. 4a, in red) exhibits a hexagonal structure of $MoSe_2$ and $Co_{0.85}Se$, indicating the successful introduction of Co element into the $MoSe_2$ thin layers. Fig. 4b-d exhibit the XPS spectra of the 2D $MoSe_2$/CoMoSe LH (in back) and $MoSe_2$/CoMoSe LH and VH (in red) atomic layers. The Mo 3d peaks ($3d_{5/2}$, 228.3 eV; $3d_{3/2}$, 231.4 eV) and Se 3d peaks ($3d_{5/2}$, 53.9 eV; $3d_{3/2}$, 54.7 eV) in Fig. 4b and d are attributed to $MoSe_2$ in accordance with the reported values.[36,37] The Co 2p core-level peaks of Co^{2+} $2p_{3/2}$, Co^{3+} $2p_{3/2}$, Co^{2+} $2p_{1/2}$ and Co^{3+} $2p_{1/2}$ are located at ~780.8, 779.0, 797.2 and 794.0 eV, respectively, as shown in Fig. 4c, which are close to the previous reports of $Co_{0.85}Se$ materials.[38,39] The Co doping levels of 2D terrace $MoSe_2$/CoMoSe LH, LH and VH nanolayers are 1.3 and 5.3 wt%, respectively. The Co content in $MoSe_2$/CoMoSe LH is obviously lower than those in $MoSe_2$/CoMoSe LH and VH. These results are consistent with the XRD results. The existence of Co 2p peaks in the products further manifest the successful Co doping in $MoSe_2$ atom layers.

To be compared with, triangular $MoSe_2$ monolayers (Fig. S2) were also grown and characterized using various techniques. Fig. S2a exhibits high density triangular $MoSe_2$ with the size of ~10 μm, which displays homogeneous color contrast in optical image. Homogeneous color indicates the high quality crystal and uniform thickness of the grown $MoSe_2$ triangles. These results are in agreement with the SEM image shown in Fig. S2b. The thickness of $MoSe_2$ triangles is ~0.7 nm, indicating that the grown $MoSe_2$ triangles are monolayers. AFM phase

View Article Online
DOI: 10.1039/C7TA02327H

image (the inset of Fig. S2f) exhibits the single $MoSe_2$ phase due to the same color contrast. The Mo 3d (Fig. S2d), Se 3d (Fig. S2e) XPS, Raman (Fig. S2g) and PL (Fig. S2h) spectra of $MoSe_2$ triangles are consistent with the previous results of $MoSe_2$ region in $MoSe_2$/CoMoSe heterostructures. The Co 2p peaks are absent in Fig. S2f, agreeing with the expectation. The schematic illustration of prospective and side views of triangular $MoSe_2$ monolayers are shown in Fig. S2i.

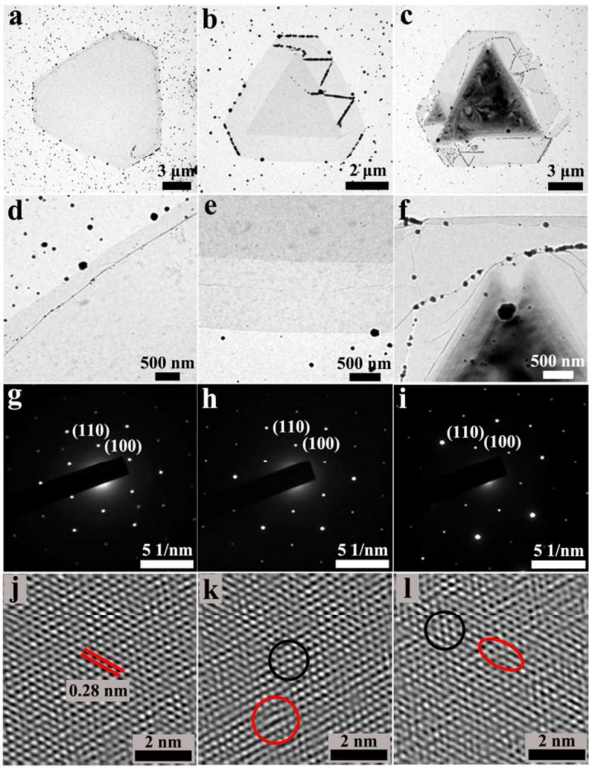

Fig. 5 TEM characterization of defective 2D terrace $MoSe_2$/CoMoSe LH, LH and VH nanolayers. Different magnification TEM images, SAED patterns and HRTEM images of 2D $MoSe_2$/CoMoSe LH (a,d,g,j), bilayer $MoSe_2$/CoMoSe LH and VH (b,e,h,k), multilayer $MoSe_2$/CoMoSe LH and VH (c,f,i,l) nanolayers.

Different magnification TEM images of defective 2D terrace $MoSe_2$/CoMoSe LH (Fig. 5a,d), bilayer (Fig. 5b,e) and multilayer (Fig. 5c,f) $MoSe_2$/CoMoSe LH and VH nanolayers show clearly the different types of $MoSe_2$/CoMoSe heterostructures with diverse number of layers through contrasting light and dark regions of the images. With the increase of the number of layer, the image color becomes darker. High magnification TEM image (Fig. 5f) of multilayer $MoSe_2$/CoMoSe LH and VH nanolayers clearly displays terrace structures of the products with more edge layers. The black nanoparticles in TEM images are the residual impurities during the transfer procedure for the as-grown nanolayers from SiO_2/Si substrate to Cu TEM grid. The elemental composition obtained from the TEM-EDX characterization (Fig. S3) of multilayer $MoSe_2$/CoMoSe LH and VH in thick core region exhibits the existence of Mo, Co and Se elements in the products. Crystalline structure of 2D $MoSe_2$/CoMoSe heterostructures was further investigated using the SAED. All SAED patterns in regions of $MoSe_2$ monolayer (Fig. 5g), bilayer $MoSe_2$/CoMoSe VH (Fig. 5h) and multilayer $MoSe_2$/CoMoSe VH (Fig. 5i) apparently display one single set of hexagonally arranged diffraction spots that can be referred to six−fold symmetry of the [001] zone axis of $MoSe_2$ lattice structure. These results reveal that there is no change of the crystalline structure of $MoSe_2$, although the doping of Co element into the $MoSe_2$ atom layers results in the formation of CoMoSe alloy. The HRTEM images in Fig. 5j-l show a lattice plane spacing of 0.28 nm which can be assigned to the (100) plane of $MoSe_2$, in consistence with the previous reports.[5,40] It is worth noting that slight atomic arrangement distortions and point defects are observed and marked with the red circles in Fig. 5k, l and S4 in some regions of HRTEM images of $MoSe_2$/CoMoSe heterostructures (dark circles display perfect crystal structure (nondefect form)), which still preserve the pristine 2D $MoSe_2$ crystalline arrangement. Slight distortions and point defects in the basal plane of 2D TMDCS atomic layers will generate more active sites to activate inert 2D basal plane for improving HER activity, since the active sites of perfect 2D TMDCS atomic layers are only existed in the edge position. And the corresponding schematic illustration is shown in Fig. S5.

Based on the succesful heterogeneous doping of the Co in the $MoSe_2$ atomic layers, there could be more active sites to be produced due to the atomic distortion in CoMoSe alloy nanolayers, thus could be beneficial for HER application combining with the Co catalysis. From literature, the heterogeneous spin states lead to the distorted atomic arrangement, and the metal ions inserted into the TMDCS atomic layers provide a fresh desired nanomaterial for optimizing HER active sites.[15] Moreover, the formation of 2D TMDCS atomic layers is crucial for the primitive electron conjugated structure on the 2D plane and beneficial to fast electron transfer for optimizing the HER performance.[15]

In order to prove the above discussions, the electrocatalytic HER performance of defective 2D terrace $MoSe_2$/CoMoSe LH, LH and VH nanolayers was investigated and the results are shown in Fig. 6. The HER measurements were performed in a three-electrode system with a 0.5 M H_2SO_4 solution. The 2D atomic layers products were transfered from SiO_2/Si substrate to GC electrode using Polymethyl Methacrylate (PMMA) solution as the working electrode. Schematic diagram of 2D atomic layer materials on the GC electrode is shown in Fig. 6a. The electrons are shifted from GC electrode to 2D atomic layers materials and finally acquired by hydrogen ions. The polarization curves for triangular $MoSe_2$ monolayers, $MoSe_2$/CoMoSe LH, $MoSe_2$/CoMoSe LH and VH nanolayers, along with those of commercial Pt/C (~0.57 mg cm^{-2}; Pt 10 %, Aladdin), and bare GC electrode for comparisons, are exhibited in Fig. 6b. All of the 2D TMDCS atomic layers exhibit low overpotentials to steer the electrode reaction, and among them, $MoSe_2$/CoMoSe LH and VH presents the lowest value of 305 mV at 10 mA cm^{-2} current density, suggesting the best HER activity. In contrast, triangular $MoSe_2$ monolayers, $MoSe_2$/CoMoSe LH displayed inadequate HER performance,

View Article Online
DOI: 10.1039/C7TA02327H

with the larger overpotentials of 378 mV and 339 mV at 10 mA cm^{-2} current density, respectively. Tafel slope was used to further assess the HER activity of the products, which is a crucial parameter that exhibits hydrogen evolution reaction dynamics. As shown in Fig. 6c, the smallest Tafel slope of ~95.2 mV dec^{-1} was calculated for the $MoSe_2$/CoMoSe LH and VH, and the obtained value is clearly smaller than those of $MoSe_2$/CoMoSe LH of ~122.3 mV dec^{-1} and triangular $MoSe_2$ monolayers of ~134.2 mV dec^{-1}. As far as we have searched in the literature, the HER activity of $MoSe_2$/CoMoSe LH and VH is comparable to the most reported value from the 2D noble-metal-free TMDCS atomic layers electrocatalysts (Table S1).

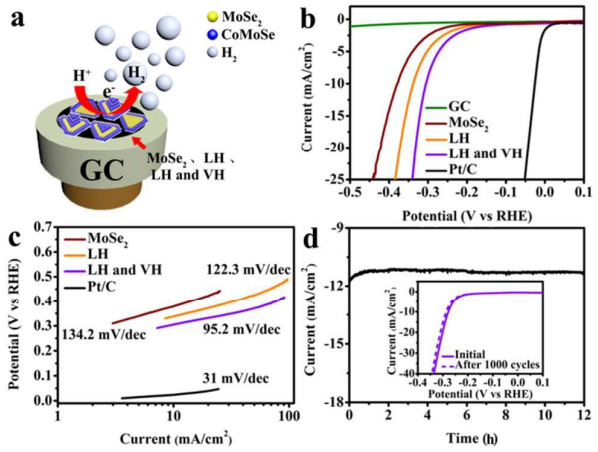

Fig. 6 Electrochemical catalytic performance of 2D triangular $MoSe_2$ monolayers, defective 2D terrace $MoSe_2$/CoMoSe LH, LH and VH nanolayers on GC electrode. (a) Schematic illustration, (b) Polarization curves after *iR* correction, (c) Tafel plots, (d) Stability testing.

The Nyquist plots (Fig. S6) show that the charge-transfer resistances (R_{ct}) of 2D triangular $MoSe_2$ monolayers, defective 2D terrace $MoSe_2$/CoMoSe LH, LH and VH nanolayers are ~239.7, 89.5, and 35.2 Ω at 310 mV overpotential (*vs.* RHE), respectively. The $MoSe_2$/CoMoSe LH and VH nanolayers exhibit the lowest R_{ct}, therefore, they are the best catalyst with the highest rate of charge transfer for all the products in this study. Apart from HER activity and conductivity, the stability of the materials is also a significant factor for the best performance of the electrocatalyst. To confirm the long-term durability of $MoSe_2$/CoMoSe LH and VH under preserve a strong-acid condition, $MoSe_2$/CoMoSe LH and VH electrocatalyst was kept in 0.5 M sulfuric acid with an overpotential of 310 mV for 12 h and cycled for 1000 cycles. As shown in Fig. 6d, a minor degradation in the current density and overpotential after stability test suggests that this electrocatalyst has an excellent stability. And the microstructure of $MoSe_2$/CoMoSe LH and VH catalyst after long-term test has slightly altered as shown in Fig. S7 and S8.

Based on the electrocatalytic measurement, the combination of good electrocatalytic parameters of small overpotential at 10 mA cm^{-2} current density, low Tafel slope, large current density, and good stability for $MoSe_2$/CoMoSe LH and VH electrocatalyst clearly prove that the formation of distorted atomic structures, 2D terrace edge layered architecture, and using more Co element catalyst in $MoSe_2$/CoMoSe LH and VH enhance the additional HER activity sites and improve HER performance.

Conclusions

In conclusion, defective 2D terrace $MoSe_2$/CoMoSe LH, bilayer and multilayer $MoSe_2$/CoMoSe LH and VH nanolayers have been successfully grown on SiO_2/Si substrate using the CVD method. The Co element was inserted into $MoSe_2$ atomic layers at a high temperature of ~900 °C to fabricate CoMoSe nanolayers, and then the 2D $MoSe_2$/CoMoSe LH and VH were obtained by the growth of CoMoSe alloy along the edge and on the surface of the $MoSe_2$ monolayers. As a result of the heterogeneous doping of Co in $MoSe_2$, more active sites were created through the atomic re-arrangement and distortion in CoMoSe alloy thin layers, atomic level coarsening in LH abutments and added terrace edge layers in VH enhancing the HER performance accompanying with metal Co element catalysis. 2D $MoSe_2$/CoMoSe LH and VH nanolayers display the lowest overpotential (305 mV) at a current density of 10 mA·cm^{-2}, the smallest Tafel slope (95.2 mV dec^{-1}) and good stability of the obtained devices under a strong-acid condition, which are comparable with those reported for the 2D TMDCS thin layer materials. It is believed that the present method is a facile yet trustworthy technique to doping other metal ions into 2D TMDCS atomic layers to generate novel types of alloy nanolayers for obtaining new LH or VH on diverse substrates, and open our mind in the development of the next generation HER electrocatalysts.

Acknowledgements

This work is supported by the National Natural Science Foundation of China (NSFC, nos. 61172001, 61390502, and 21373068), and the National Key Basic Research Program of China (973 Program) under Grant no. 2013CB632900, and by the Foundation for Innovative Research Groups of the National Natural Science Foundation of China (Grant no. 51521003) and by Self-Planned Task (no. SKLRS201607B) of State Key Laboratory of Robotics and System (HIT), as well as the UK Engineering and Physical Sciences Research Council (EPSRC) EP/P018998/1.

Notes and references

1 M. Mahjouri-Samani, M. W. Lin, K. Wang, A. R. Lupini, J. Lee, L. Basile, A. Boulesbaa, C. M. Rouleau, A. A. Puretzky, I. N. Ivanov, K. Xiao, M. Yoon and D. B. Geohegan, *Nat. Commun.*, 2015, **6,** 7749.
2 W. Zheng, W. Feng, X. Zhang, X. S. Chen, G. B. Liu, Y. F. Qiu, T. Hasan, P. H. Tan and P. A. Hu, *Adv. Funct. Mater.*, 2016, **26,** 2648-2654.
3 X. S. Chen, G. B. Liu, W. Zheng, W. Feng, W. W. Cao, W. P. Hu and P. A. Hu, *Adv. Funct. Mater.*, 2016, **26,** 8537-8544.

View Article Online
DOI: 10.1039/C7TA02327H

4 W. Zheng, J. H. Lin, W. Feng, K. Xiao, Y. F. Qiu, X. S. Chen, G. B. Liu, W. W. Cao, S. T. Pantelides, W. Zhou and P. A. Hu, *Adv. Funct. Mater.*, 2016, **26**, 6371-6379.

5 X. D. Duan, C. Wang, J. C. Shaw, R. Cheng, Y. Chen, H. L. Li, X. P. Wu, Y. Tang, Q. L. Zhang, A. L. Pan, J. H. Jiang, R. Q. Yu, Y. Huang and X. F. Duan, *Nat. Nanotech.*, 2014, **9,** 1024-1030.

6 J. M. Woods, Y. Jung, Y. J. Xie, W. Liu, Y. H. Liu, H. H. Wang and J. J. Cha, *Acs Nano*, 2016, **10,** 2004-2009.

7 H. Fang, C. Battaglia, C. Carraro, S. Nemsak, B. Ozdol, J. S. Kang, H. A. Bechtel, S. B. Desai, F. Kronast, A. A. Unal, G. Conti, C. Conlon, G. K. Palsson, M. C. Martin, A. M. Minor, C. S. Fadley, E. Yablonovitch, R. Maboudian and A. Javey, *Proc. Natl. Acad. Sci. U.S.A.*, 2014, **111,** 6198-6202.

8 D. Voiry, H. Yamaguchi, J. W. Li, R. Silva, D. C. B. Alves, T. Fujita, M. W. Chen, T. Asefa, V. B. Shenoy, G. Eda and M. Chhowalla, *Nat. Mater.*, 2013, **12,** 850-855.

9 B. L. Liu, Y. Q. Ma, A. Y. Zhang, L. Chen, A. N. Abbas, Y. H. Liu, C. F. Shen, H. C. Wan and C. W. Zhou, *Acs Nano*, 2016, **10,** 5153-5160.

10 H. L. Li, Q. L. Zhang, X. D. Duan, X. P. Wu, X. P. Fan, X. L. Zhu, X. J. Zhuang, W. Hu, H. Zhou, A. L. Pan and X. F. Duan, *J. Am. Chem. Soc.*, 2015, **137,** 5284-5287.

11 Y. Liu, N. O. Weiss, X. D. Duan, H. C. Cheng, Y. Huang and X. F. Duan, *Nat. Rev. Mater.*, 2016, **1,** 16042.

12 L. Samad, S. M. Bladow, Q. Ding, J. Q. Zhuo, R. M. Jacobberger, M. S. Arnold and S. Jin, *Acs Nano*, 2016, **10,** 7039-7046.

13 Q. Fu, L. Yang, W. H. Wang, A. Han, J. Huang, P. W. Du, Z. Y. Fan, J. Y. Zhang and B. Xiang, *Adv. Mater.*, 2015, **27,** 4732-4738.

14 X. S. Chen, Z. G. Wang, Y. F. Qiu, J. Zhang, G.B. Liu, W. Zheng, W. Feng, W. W. Cao, P. A. Hu and W. P. Hu, *J. Mater. Chem. A*, 2016, **4,** 18060-18066.

15 Y. W. Liu, X. M. Hua, C. Xiao, T. F. Zhou, P. C. Huang, Z. P. Guo, B. C. Pan and Y. Xie, *J. Am. Chem. Soc.*, 2016, **138,** 5087-5092.

16 Y. Zhang, X. S. Chen, Y. Huang, C. Zhang, F. Li and H. B. Shu, *J. Phys. Chem. C*, 2017, **121,** 1530-1536.

17 L. X. Lin, N. H. Miao, Y. Wen, S. W. Zhang, P. Ghosez, Z. M. Sun and D. A. Allwood, *Acs Nano*, 2016, **10,** 8929-8937.

18 M. Mahjouri-Samani, L. B. Liang, A. Oyedele, Y. S. Kim, M. K. Tian, N. Cross, K. Wang, M. W. Lin, A. Boulesbaa, C. M. Rouleau, A. A. Puretzky, K. Xiao, M. Yoon, G. Eres, G. Duscher, B. G. Sumpter and D. B. Geohegan, *Nano Lett.*, 2016, **16,** 5213-5220.

19 X. F. Li, M. W. Lin, L. Basile, S. M. Hus, A. A. Puretzky, J. Lee, Y. C. Kuo, L. Y. Chang, K. Wang, J. C. Idrobo, A. P. Li, C. H. Chen, C. M. Rouleau, D. B. Geohegan and K. Xiao, *Adv. Mater.*, 2016, **28,** 8240.

20 H. J. Chuang, B. Chamlagain, M. Koehler, M. M. Perera, J. Q. Yan, D. Mandrus, D. Tomanek and Z. X. Zhou, *Nano Lett.*, 2016, **16,** 1896-1902.

21 X. S. Chen, Y. F. Qiu, H. H. Yang, G. B. Liu, W. Zheng, W. Feng, W. W. Cao, W. P. Hu and P. A. Hu, *ACS Appl. Mater. Inter.*, 2017, **9,** 1684-1691.

22 J. Staszak-Jirkovsky, C. D. Malliakas, P. P. Lopes, N. Danilovic, S. S. Kota, K. C. Chang, B. Genorio, D. Strmcnik, V. R. Stamenkovic, M. G. Kanatzidis and N. M. Markovic, *Nat. Mater.*, 2016, **15,** 197-204.

23 N. Kornienko, J. Resasco, N. Becknell, C. M. Jian, Y. S. Liu, K. Q. Nie, X. H. Sun, J. H. Guo, S. R. Leone and P. D. Yang, *J. Am. Chem. Soc.*, 2015, **137,** 7448-7455.

24 Y. Ito, W. T. Cong, T. Fujita, Z. Tang and M. W. Chen, *Angew. Chem.*, 2015, **54,** 2131-2136.

25 X. D. Yan, L. H. Tian, M. He and X. B. Chen, *Nano Lett.*, 2015, **15,** 6015-6021.

26 D. S. Kong, H. T. Wang, Z. Y. Lu and Y. Cui, *J. Am. Chem. Soc.*, 2014, **136,** 4897-4900.

27 G. B. Liu, Z. H. Li, T. Hasan, X. S. Chen, W. Zheng, W. Feng, D. C. Jia, Y. Zhou and P. A. Hu, *J. Mater. Chem. A*, 2017, **5,** 1989-1995.

28 Y. Li, L. Zhang, X. Xiang, D. P. Yan and F. Li, *J. Mater. Chem. A*, 2014, **2**, 13250-13258.

29 L. Zhang, W. H. He, X. Xiang, Y. Li and F. Li, *RSC Adv.*, 2014, **4,** 43357-43365.

30 W. H. He, R. R. Wang, L. Zhang, J. Zhu, X. Xiang and F. Li, *J. Mater. Chem. A*, 2015, **3**, 17977-17982.

31 J. P. Shi, D. L. Ma, G. F. Han, Y. Zhang, Q. Q. Ji, T. Gao, J. Y. Sun, X. J. Song, C. Li, Y. S. Zhang, X. Y. Lang, Y. F. Zhang and Z. F. Liu, *Acs Nano*, 2014, **8,** 10196-10204.

32 Y. F. Yu, S. Y. Huang, Y. P. Li, S. N. Steinmann, W. T. Yang and L. Y. Cao, *Nano Lett.*, 2014, **14,** 553-558.

33 L. Yang, Q. Fu, W. H. Wang, J. Huang, J. L. Huang, J. Y. Zhang and B. Xiang, *Nanoscale*, 2015, **7,** 10490-10497.

34 W. Park, J. Baik, T. Y. Kim, K. Cho, W. K. Hong, H. J. Shin and T. Lee, *Acs Nano*, 2014, **8,** 4961-4968.

35 C. Lee, H. Yan, L. E. Brus, T. F. Heinz, J. Hone and S. Ryu, *Acs Nano*, 2010, **4,** 2695-2700.

36 G. W. Shim, K. Yoo, S. B. Seo, J. Shin, D. Y. Jung, I. S. Kang, C. W. Ahn, B. J. Cho and S. Y. Choi, *Acs Nano*, 2014, **8,** 6655-6662.

37 X. L. Wang, Y. J. Gong, G. Shi, W. L. Chow, K. Keyshar, G. L. Ye, R. Vajtai, J. Lou, Z. Liu, E. Ringe, B. K. Tay and P. M. Ajayan, *Acs Nano*, 2014, **8,** 5125-5131.

38 Z. X. Zhang, X. W. Wang, K. L. Wu, Y. X. Yue, M. L. Zhao, J. Cheng, J. Ming, C. J. Yu and X. W. Wei, *New J. Chem.*, 2014, **38,** 6147-6151.

39 Z. H. Wang, Q. Sha, F. W. Zhang, J. Pu and W. Zhang, *CrystEngComm*, 2013, **15,** 5928-5934.

40 J. Xia, X. Huang, L. Z. Liu, M. Wang, L. Wang, B. Huang, D. D. Zhu, J. J. Li, C. Z. Gu and X. M. Meng, *Nanoscale*, 2014, **6,** 8949-8955.

View Article Online
DOI: 10.1039/C7TA02327H

Tuning electrochemical catalytic activity of defective 2D terrace $MoSe_2$ heterogeneous catalyst *via* cobalt doping

ToC figure

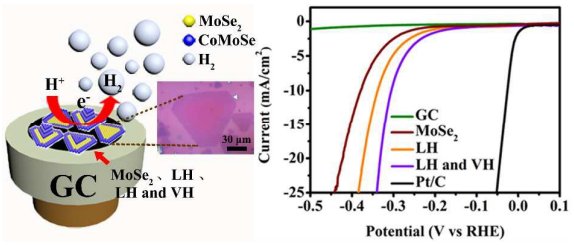

Defective 2D terrace $MoSe_2$/CoMoSe lateral and vertical heterostructures nanolayers electrocatalyst *via* metal cobalt doping displays ameliorative HER activity.